

# Untangling the Mistral and Seasonal Atmospheric Forcing Driving Deep Convection in the Gulf of Lion: 1993-2013

Douglas Keller Jr.<sup>1</sup>, Yonatan Givon<sup>2</sup>, Romain Pennel<sup>1</sup>, Shira Raveh-Rubin<sup>2</sup>,  
Philippe Drobinski<sup>1</sup>

<sup>1</sup>LMD/IPSL, École Polytechnique, Institut Polytechnique de Paris, ENS, PSL Research University,  
Sorbonne Université, CNRS, Palaiseau, France

<sup>2</sup>Department of Earth and Planetary Sciences, Weizmann Institute of Science, Rehovot, Israel

## Key Points:

- Winters with deep convection have below average levels of stratification that the atmospheric forcing has to overcome.
- The seasonal atmospheric change is the main driver of destratification.
- The Mistral winds have a low frequency signature that elevates the seasonal wind speeds in the winter.

---

Corresponding author: Douglas Keller Jr., [dg.kllr.jr@gmail.com](mailto:dg.kllr.jr@gmail.com)

## Abstract

Deep convection occurs periodically in the Gulf of Lion, driven by the seasonal atmospheric change and Mistral winds. To determine the variability and drivers of the seasonal and Mistral forcing, 20 years of ocean simulations were run. Two sets of simulations were performed: a control set, forced by unfiltered atmospheric forcing, and a seasonal set, forced by filtered forcing. The filtered forcing retained the seasonal aspects but removed the high frequency phenomena. Assuming the Mistral acts primarily in the high frequency, comparing the two sets allows for distinguishing the effects of the Mistral on the ocean response. During the preconditioning phase, the seasonal forcing was found to be the main destratifying process, removing on average 45.7% of the stratification, versus the 28.0% removed by the Mistral. Despite this difference, at the time of deep convection, both the seasonal and Mistral forcing each triggered deep convection in roughly half of the events. Larger sensible and latent heat fluxes were found in the seasonal forcing of the years with deep convection, acting as the main drivers (removing  $0.17 \text{ m}^2\text{s}^{-2}$  and  $0.43 \text{ m}^2\text{s}^{-2}$  of stratification, respectively). They are themselves driven by increased wind speeds, believed to be the low frequency signal of the Mistral, as more Mistral events occur during winters with deep convection (34.3% versus 28.6%). The evolution of the seasonal forcing in a changing climate may have a significant effect on the future deep convection cycle of the Gulf of Lion.

## Plain Language Summary

Deep convection occurs periodically in the Gulf of Lion, when water at the surface of the ocean is cooled enough to mix freely with the deeper water below, sometimes reaching the sea floor. It is an important part of the overall circulation of the Mediterranean Sea that leads to an explosion in the phytoplankton population when it occurs. In the gulf, the surface cooling is caused by the seasonal atmospheric change and the Mistral winds. The latter is a cool, dry northerly flow that flows through the Rhône Valley out over the gulf. In our study, we ran ocean simulations that included and excluded the non-seasonal effects of the Mistral to determine the importance of the seasonal atmospheric change and Mistral on deep convection. We found that the seasonal atmospheric change has a larger role in cooling the ocean surface, with part of the Mistral acting on the seasonal timescale, elevating the average wind speeds found during the winter. Changes in the seasonal atmospheric change and composition of the ocean waters will need to be studied to understand the evolution of deep convection in the gulf and its consequences on the Mediterranean Sea dynamics and biology in a changing climate.

## 1 Introduction

Deep convection, or open-ocean convection, occurs in the higher latitude regions of the world and is an important ocean circulation process (Marshall & Schott, 1999). It is formed when the stable density gradient along the ocean column is eroded by surface buoyancy loss, leading to an overturning that can span the entire depth of the column. In the western basin of the Mediterranean Sea (Med. Sea), this process can occur in the Gulf of Lion (GOL) and assists in the thermohaline circulation of the sea (Robinson et al., 2001) by forming the Western Mediterranean Deep Water (WMDW). When it does occur, the WMDW produced spreads out along the bottom of the northwest basin (MEDOC, 1970). Some is transported along the northern boundary current towards the Balearic Islands (Send & Testor, 2017), and some of it completes the general circulation by flowing down towards the Algerian Basin and the Strait of Gibraltar (Beuvier et al., 2012; Testor & Gascard, 2003). In the GOL, deep convection also plays an important role in the marine biology of the region, as the springs following deep convection events also experience increased phytoplankton blooming (Severin et al., 2017), due to the increased



levels of nutrients and oxygenation from the mixing process (Coppola et al., 2017; Severin et al., 2017).

Significant deep convection events occur every few years in the GOL (Bosse et al., 2021; Somot et al., 2016; Houpert et al., 2016; Marshall & Schott, 1999; Mertens & Schott, 1998), driven by the Mistral and Tramontane winds. These sister, northerly flows bring cool, continental air through the Rhône Valley (Mistral) and the Aude Valley (Tramontane), leading to large heat transfer events with the warmer ocean surface (Drobinski et al., 2017; Flamant, 2003). These large cooling, evaporative events destabilize the water column in the GOL, and are a primary source of buoyancy loss leading to deep convection (Lebeaupin-Brossier et al., 2017; Houpert et al., 2016; L'Hévéder et al., 2012; Lebeaupin-Brossier et al., 2012; Herrmann et al., 2010; Lebeaupin-Brossier & Drobinski, 2009; Noh et al., 2003; Marshall & Schott, 1999; Mertens & Schott, 1998; Madec et al., 1996; Schott et al., 1996; Madec, Delecluse, et al., 1991; Madec, Chartier, & Crépon, 1991; Gascard, 1978). The other main source of buoyancy loss in the region is the seasonal atmospheric change and reduction of solar heating during the winter (Keller Jr. et al., 2022).

The annual stratification cycle of the GOL regulates the occurrence of deep convection events. It comprises of a destratification phase and restratification phase that is roughly sinusoidal in appearance. These two phases form due to the net heat flux into the ocean surface changing sign roughly at the spring and fall equinoxes: positive between March and September and negative between September and March. When the net heat flux is positive, the ocean column is being heated, increasing its stability, hence an increase in stratification from March to September. When the net heat flux is negative, the ocean column is being cooled, reducing its stability, thereby decreasing its stratification from September and March. The net heat flux gains its shape from its four main components: solar heating, infrared cooling, the sensible heat flux, and the latent heat flux. The solar heating gives the net heat flux its sinusoidal shape. The infrared cooling, sensible heat flux, and latent heat flux shift this sinusoidal shape negative, causing it to flip sign at the spring and fall equinoxes. The asymmetries in the net heat flux come from the sensible and latent heat fluxes, causing the sinusoidal shape to be distorted slightly in the winter (Keller Jr. et al., 2022).

If the cooling from the sensible and latent heat fluxes is large enough (the infrared cooling tends to remain constant as it depends on the sea surface temperature), then a third phase appears: the deep convection phase. This occurs when the sensible and latent heat fluxes reduce the stratification to point it can overturn. These three phases then form the canonical deep convection cycle (MEDOC, 1970; The Lab Sea Group, 1998), where the destratification phase is typically referred to as the preconditioning phase. For this study, we are focusing on the destratification/preconditioning and deep convection phases, as they drive the variability of this cycle in the GOL.

In a sister paper, Keller Jr. et al. (2022), we determined the importance of the seasonal atmospheric change with regards to its impact on the destratification phase and discovered it was a more significant source of destratification than the Mistral/Tramontane winds (referred to as just the Mistral), providing roughly 2/3 of the destratification for the 2012 to 2013 winter. The current study continues this investigation and looks into the variability of the contribution to destratification for each component, the seasonal and the Mistral, over multiple years. 20 years of the Med. Sea, from July 1st, 1993 to June 30th, 2013, were simulated using the NEMO ocean model. NEMO was driven by two sets of WRF/ORCHIDEE atmospheric data: a control set and a filtered (seasonal) set. This resulted in two sets of the simulated ocean data: one set including the effects of the Mistral and the seasonal effects, and the other set just including the seasonal effects, allowing us to separate the effects due to the Mistral.

In particular, our findings determine:

- the variability of both the seasonal and Mistral based contributions to destratification,
- and the primary components, and their drivers, of the seasonal contribution leading to deep convection.

Our findings also address questions posed by Keller Jr. et al. (2022) that were outside the scope of that study. These questions can be summarized as the following:

1. Does the Mistral trigger deep convection, or does the seasonal change trigger it?
2. Does the maximum  $SI_S$  play a role in deep convection?
3. Does the timing of the  $SI_S$  minimum matter and can the Mistral contribution overcome a restratifying  $SI_S$ ?
4. Does the previous year's stratification affect the proceeding year?

The paper is organized in the following way. The NEMO model, atmospheric forcing data and filtering, additional methodology, and observational data are described in the Methodology section (Sec. 2). The ocean model outputs are validated using the observational data in the Model Validation section (Sec. 3). The results of the seasonal and Mistral contributions are presented and discussed in the Results and Discussion section (Sec. 4), along with addressing the posed by Keller Jr. et al. (2022). Concluding the paper is the Conclusions section (Sec. 5).

## 2 Methodology

To separate the effect of the Mistral and seasonal aspects of the atmospheric forcing, two sets of ocean simulations simulating the Med. Sea were carried out: one control set and one seasonal set. The seasonal set had part of its atmospheric forcing filtered to remove the Mistral from the forcing, thereby allowing the differences between the two ocean simulation sets to reflect the effect the Mistral has on the ocean. As the Mistral is the main intra-monthly phenomenon that occurs during the winter in the GOL (Keller Jr. et al., 2022; Givon et al., 2021), the seasonal ocean simulations reflect the ocean response just due to the seasonal atmospheric changes in the region. The two ocean simulation sets are performed on a per year basis from the same initial conditions. For example, one control and seasonal simulation pair was run from July 1st, 1993 to June 30th, 1994. The same was performed from July 1st, 1994 to June 30th, 1995 and so on, until June 30th, 2013. This was done to allow for the assumption that processes outside the NW Med. subdomain in Fig. 1 (b) that are affected by the filtering, have a negligible impact on the GOL processes during the comparison of per year ocean simulations. This assumption is corroborated by the slow movement of intermediate and dense water, which is on the order of two years for intermediate waters to travel from the Strait of Sicily to the GOL (Amitai et al., 2021). It is also corroborated by the roughly year time scale for newly formed WMDW (Western Mediterranean Deep Water) to move into the southern Algerian Basin (Beuvier et al., 2012) and the order of decades time scale for total circulation of the Med. Sea (Milot & Taupier-Letage, 2005).

### 2.1 NEMO

The Nucleus for European Modelling of the Ocean (NEMO) ocean model (<https://www.nemo-ocean.eu/>; last accessed: August 16th, 2022) was used to simulate the Med. Sea in one year runs for 20 years, as described above, from July 1st, 1993 to June 30th, 2013. The model was run in bulk configuration, utilizing the following parameterized equations:

$$Q_E = \rho_{a,0} \Lambda C_E (\Delta q) |\Delta \vec{u}| \quad (1)$$

$$Q_H = \rho_{a,0} c_p C_H (\Delta \theta) |\Delta \vec{u}| \quad (2)$$

$$Q_{LW} = Q_{LW,a} - \epsilon \sigma SST_K^4 \quad (3)$$

$$\tau = \rho_{a,0} C_D \Delta \vec{u} |\Delta \vec{u}| \quad (4)$$

Where  $Q_E$ ,  $Q_H$ ,  $Q_{LW}$ , and  $\tau$  are the latent heat, sensible heat, longwave radiation fluxes and the surface shear stress, respectively.  $z$  is the height above the sea surface where the atmospheric variables are provided at, with the naught values ( $_0$ ) at the sea surface.  $\vec{u}$  is the horizontal wind vector, with  $\Delta \vec{u} = \vec{u}_z - \vec{u}_0$  as the difference between the wind velocity and sea surface current.  $\Delta q = q_z - q_0$  and  $\Delta \theta = \theta_z - SST$ ;  $q$  and  $\theta$  are the specific humidity and potential temperature of air, respectively.  $\Lambda$  and  $c_p$  are the latent heat of evaporation and the specific heat of water, respectively.  $\rho_a$  is the density of air.  $SST_K$  is the sea surface absolute temperature.  $\epsilon$  is the sea surface emissivity,  $\sigma$  is the Stefan-Boltzmann constant, and  $Q_{LW,a}$  is the atmospheric longwave radiation. The coefficients  $C_E$ ,  $C_H$ , and  $C_D$  are the parameterized coefficients of latent heat, sensible heat, and drag, respectively, and are defined in W. Large and Yeager (2004) and W. G. Large and Yeager (2008).

$Q_{net}$ , the net downward heat flux, is the summation of the components in the following equation ((W. Large & Yeager, 2004) and (Estournel et al., 2016); ignoring snow-fall):

$$Q_{net} = Q_{SW} + Q_{LW} + Q_H + Q_E \quad (5)$$

Where  $Q_{SW}$  is the downward shortwave radiation.

The NEMO model was also run in the NEMOMED12 configuration, using NEMO v3.6. NEMOMED12 is described, with boundary conditions, in Waldman et al. (2018); Hamon et al. (2016); Beuvier et al. (2012); Lebeaupin-Brossier et al. (2011); a brief description follows: the domain covers the Med. Sea and a portion of the Atlantic Ocean (see Fig. 1 (b)). The latter buffer zone is used to represent the exchanges between the two bodies of water at the Strait of Gibraltar, and its sea surface height (SSH) fields are restored towards the ORAS4 global ocean reanalysis (Balmaseda et al., 2013). The 3-D temperature and salinity fields of the buffer zone are restored towards the MEDRYS reanalysis (Hamon et al., 2016). The Black Sea, runoff of 33 major rivers, and coastal runoff are represented by climatological data from Ludwig et al. (2009). The initial conditions for each one year run were pulled from the MEDRYS reanalysis (Hamon et al., 2016).

## 2.2 Atmospheric Forcing

The atmospheric forcing used in the simulations were the output of a RegIPSL simulation, the regional climate model of IPSL (Guion et al., 2021) (<https://gitlab.in2p3.fr/ipsl/lmd/intro/regips1/regips1>; last accessed: Aug. 26th, 2022), which used the coupling of the Weather Research and Forecasting Model (WRF) (Skamarock et al., 2008) and the ORCHIDEE Land Surface Model (Krinner et al., 2005). The run is a hind-cast simulation (ERA Interim downscaling), performed at 20 km resolution, spanning the period of 1979 to 2016, within the HyMeX (Drobinski et al., 2014) and Med-CORDEX framework (Ruti et al., 2016). The  $u$  and  $v$  wind components, specific humidity, potential temperature, shortwave and longwave downward radiation, precipitation, and snow-fall were all used to force the NEMO ocean simulations.

For the control simulation set, the forcing were used as is. For the seasonal simulation set, the  $u$  and  $v$  wind components, specific humidity, and potential temperature

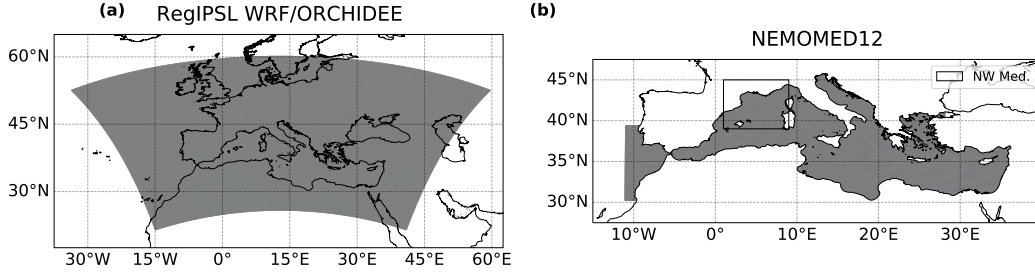


**Figure 1.** The domains of both the WRF domain from the RegIPSL coupled WRF/ORCHIDEE simulation within the Med-CORDEX framework, (a), and the NEMOMED12 configuration domain, (b). The region of interest, the NW Med., is outlined by the box. This region is later used in Fig. 3.

were filtered over the entire domain of the WRF forcing (Fig. 1 (a)). These variables are the primary variables in the surface flux calculations in the bulk formulae (Eq. set 4) that are modified by the Mistral, and are thus integral to filtering out the Mistral. The variables relating to the radiation and precipitation fluxes were left unchanged. The filtering process was performed by a moving window average:

$$\chi_i = \frac{1}{i + N + 1} \sum_{j=0}^{i+N} x_j \quad (6)$$

Where  $\chi_i$  is the averaged (filtered) value at index  $i$  of a time series of variable  $x$  with length  $n$ , where  $i = 0 \rightarrow n$ . The window size is equal to  $2N + 1$ , which, in this case, is equal to 31 days. The ends have a reduced window size for averaging, and thus show edge effects. The edge effects did not affect the forcing used for the NEMO simulations, as they were before and after the overall ocean simulation beginning and end dates.

The moving window average was applied to each time point per day over a 31 day window. I.e., for 3 hourly data, the time series is split into 8 separate series, one for each timestamp per day, (00:00, 03:00, 06:00, etc.) and then each series is averaged with a moving window. The 8 window averaged series are then recombined into a single time series. This was done to retain the intra-day variability, yet smooth the intra-monthly patterns, as the diurnal cycle has been shown to retard destratification by temporarily reforming a stratified layer at the sea surface during slight daytime warming. This diurnal restratification has to be overcome first before additional destratification of the water column can continue during the next day (Lebeaupin-Brossier et al., 2012, 2011) and is shorter than a typical Mistral event length of a little over 5 days (Keller Jr. et al., 2022). An example of the filtering can be seen in Fig. 2 of Keller Jr. et al. (2022). The filtering removes the short term, anomaly scale forcing from the forcing dataset (the phenomena with under a month timescale), effectively removing the Mistral's influence on the ocean response. This creates two separate forcing datasets: one with the anomaly forcing included, attributed to the Mistral and hence called the Mistral forcing, and one with just the seasonal forcing, leading to the designation of "control" and "seasonal" for the unfiltered and filtered datasets, respectively.

The main assumption of performing this filtering is the Mistral primarily acts on the short term, anomaly scale forcing (high frequency forcing). This found to be a fairly effective assumption when separating Mistral and seasonal effects in Keller Jr. et al. (2022).

However, there is a seasonal component to the Mistral forcing that is not removed with this filtering. Mistral events occur more frequently in the winter than in summer (Givon et al., 2021), which appears in lower frequencies of the atmospheric forcing. This will be discussed more in Sec. 4.1.1.

### 2.3 Stratification Index

The stratification index,  $SI$ , is a useful measure of the stability of the ocean column. It builds from the non penetrative growth of the mixed layer, a reasonable assumption for the ocean mixed layer (Keller Jr. et al., 2022; Somot, 2005; Turner, 1973). It compresses the Brunt-Väisälä frequency,  $N^2$ , over the depth of the water column into a single index:

$$SI = \int_0^D N^2 z dz \quad (7)$$

Where  $z$  is the depth and  $D$  is the depth of ocean column. If  $N^2$  is assumed to be constant throughout the column, the integral simplifies to:

$$SI = \frac{D^2}{2} N^2 \quad (8)$$

As  $N^2$  is proportional to the vertical density gradient,  $SI$  provides a 0 dimensional metric to measure the stratification of the ocean column. We will use it to track the stratification of the GOL and the occurrences of deep convection. Consequently, the stratification indexes from the control and seasonal simulation sets are  $SI$  and  $SI_S$ , respectively, with the difference,  $\delta SI = SI - SI_S$ , being the stratification induced by the Mistral.

### 2.4 Simple Model

To separate the different seasonal drivers of deep convection, a simple model that relates the seasonal stratification index,  $SI_S$ , to the seasonal net surface heat flux,  $Q_{net,S}$  is used (Keller Jr. et al. (2022) Eq. (16)):

$$\frac{\partial SI_S}{\partial t} = \frac{g}{2\rho c_p T_0} Q_{net,S} \approx 10^{-9} \times Q_{net,S} \quad (9)$$

Where  $c_p$  is the specific heat capacity of water (taken as  $4184 \text{ J kg}^{-1} \text{ K}^{-1}$ ),  $g$  is gravity (taken as  $9.81 \text{ ms}^{-1}$ ),  $\rho$  is the reference density of water (taken as  $1000 \text{ kg m}^{-3}$ ), and  $T_0$  is the reference temperature (taken as  $290 \text{ K}$ ; the average seasonal sea surface temperature over the 20 year period). Utilizing these values,  $\frac{g}{2\rho c_p T_0} \approx 10^{-9} \text{ m}^4 \text{ Js}^{-2}$ .  $Q_{net,S}$  can be further separated into its individual,  $i$ , components through Eq. 5, allowing us to estimate the components' individual contribution to destratification/restratification by integrating over a selected interval of time ( $t_0$  to  $t_1$ ):

$$SI_{Est,i} = 10^{-9} \times \int_{t_0}^{t_1} Q_i dt \quad (10)$$

Similarly, the effect of a Mistral event,  $k$ , on destratification,  $\delta SI_k$ , can be calculated using Eq. 17 from Keller Jr. et al. (2022):

$$\Delta \delta SI_k = \delta SI_k(t_k + \Delta t_k) - \delta SI_{k-1}(t_k) = \left[ \delta SI_{k-1}(t_k) + \frac{D^2}{2} \frac{\delta F_k}{\alpha_d} \right] (e^{-\alpha_d \Delta t_k} - 1) \quad (11)$$

Where  $t_k$  is the beginning of the event,  $\Delta t_k$  is the duration of the event,  $\delta F_k$  is the strength of the event (essentially the heat flux), and  $\alpha_d$  is the restoration coefficient, effectively the horizontal gradient of  $\delta SI$  during the event (see the Appendix of Keller Jr. et al. (2022) for more details).

## 2.5 Mistral Events

To use Eq. 11 and investigate more into how the Mistral affects the GOL, the Mistral events during the July 1st, 1993 to June 30th, 2013 period are pulled from the Mistral dataset provided by Keller Jr. et al. (2022) and Givon et al. (2021) (<https://medcyclones.utad.pt/data/>; last accessed Aug. 23rd, 2022). Mistral events are essentially determined by the simultaneous presence of northerly flows in the Rhône Valley and over the Gulf of Lion, in conjunction with a low pressure system over the Ligurian Sea. More details are provided in Keller Jr. et al. (2022) and Givon et al. (2021).

## 2.6 Argo and CTD Profiles

To validate the control set of the ocean simulations, Argo and CTD vertical profile observations from the period of July 1st, 1993 to June 30th, 2013 were collected from the Coriolis database (<https://www.coriolis.eu.org/Data-Products/Data-selection>; last accessed: Aug. 23rd, 2022). These vertical profiles were compared to the model vertical profiles to determine and verify the accuracy of the model. The model outputs salinity in terms of practical salinity, in units of *PSU*, which is the same as the observational data. However, for temperature, the model outputs potential temperature, whereas the observed temperature is provided in terms of in situ temperature measurements. To make a direct comparison, the observational temperature data was converted to potential temperature with the **GSW-Python** python package (Firing et al., 2021), which uses the TEOS-10 ocean equation of state for the conversion (<https://www.teos-10.org/index.htm>; last accessed Aug. 23rd, 2022).

## 3 Model Validation

2929 temperature and salinity in situ profiles were taken from the Coriolis database to validate the control set of the ocean simulations. 1949 profiles were from Argo profiling and 980 were from CTD profiling (breakdown in Table 1). Each profile of calculated potential temperature (see Sec. 2.6) and salinity was then compared to the model profile from the nearest grid point in the NEMOMED12 grid and nearest time stamp (daily temporal resolution for the ocean simulation data; the model data was interpolated vertically to match the levels of the observations). The bias (model minus observation) and root mean squared error (RMSE) were calculated from the comparisons.

To look at the vertical distribution of bias and RMSE, the observations and nearest model data were vertically binned (55 bins) according to depth. The bias was then calculated per observation/model result pair. The mean and standard deviation of the bias per each bin are plotted in Fig. 2 (a) and (b), for potential temperature and salinity, respectively. For each bin, the RMSE was computed, and is shown in Fig. 2 (c) and (d), for potential temperature and salinity, respectively.

As seen in Fig. 2, most of the differences between the model and observations lie within the first 500 *m* of the ocean column. The largest differences and variability in the bias are found at the surface, with a mean bias and RMSE of +0.40 °C and 1.18 °C, for potential temperature, and -0.04 *PSU* and 0.01 *PSU*, for salinity. Below 500 *m*, the bias and RMSE are much smaller, with the mean bias and RMSE averaging at -0.006 °C and 0.081 °C, for potential temperature, and +0.004 *PSU* and 0.021 *PSU*, for salinity. The larger differences in the upper 500 *m* can be explained by the diurnal cycle that isn't captured in the daily temporal resolution of the model data. The sea surface layer destrat-

**Table 1.** Number of and start and end dates for the Argo and CTD profiles from the Coriolis database for the July 1st, 1993, to June 30th, 2013. The number of profiles used for the spatial distribution of bias in the layers above and below 500 *m* in depth are shown in their respective columns.

	Start	End	Above 500 <i>m</i>	Below 500 <i>m</i>	Total
Argo	2005-01-01 08:10	2011-12-30 23:56	1948	1493	1949
CTD	1993-07-05 07:43	2013-06-29 13:02	978	236	980
Total	—	—	2926	1729	2929

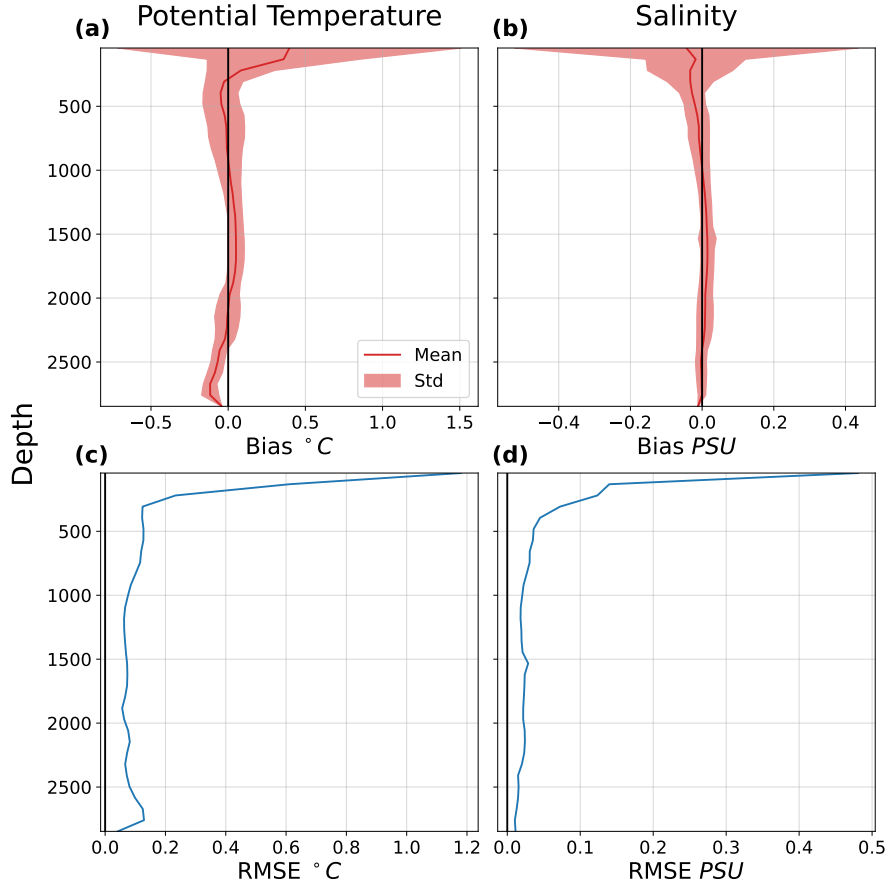


**Figure 2.** Vertical distribution of bias (model minus observation) and RMSE from the comparison of our control set model results and combined Argo/CTD observations. (a) and (b) show the mean and standard deviation of the bias for potential temperature and salinity, respectively. The mean is the solid red line, with the shading representing the area encompassed by  $\pm 1$  standard deviation. (c) and (d) show the RMSE for potential temperature and salinity, respectively.



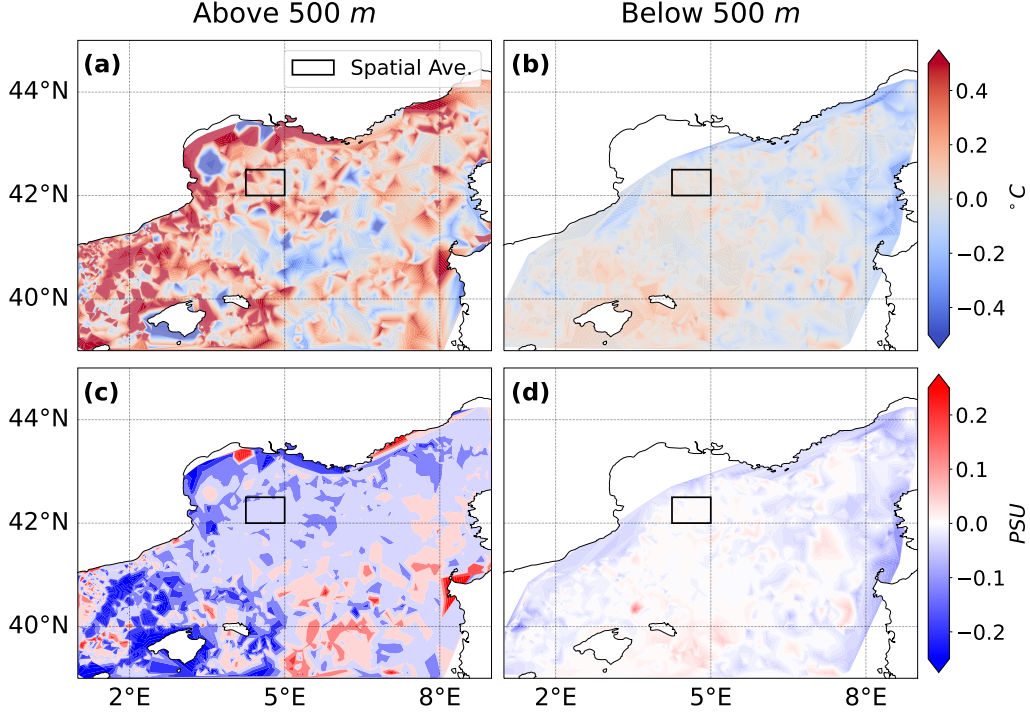


**Figure 3.** Spatial distribution of the bias from the comparison of our control set model results and combined Argo/CTD observations. (a) and (b) show the bias in the potential temperature for the layers above and below 500 *m*, respectively. (c) and (d) show the same for salinity. The black box from 42 to 42.5 °N and from 4.25 to 5 °E bounds the spatial averaging performed in Sec. 4.

ifies and restratifies with the diurnal cycle, as noted by Lebeaupin-Brossier et al. (2012, 2011), whereas the lower layers are less effected, hence showing less error between the observations and model output. With that caveat noted, the model is fairly representative of the vertical column in the GOL, with slightly warmer and fresher surface waters relative to observations and fairly accurate temperature and salinity for the deeper waters.

To see if there is any notable features in the spatial distribution of bias, the averaged bias of the water above and below 500 *m* are plotted in Fig. 3, with subplots (a) and (c) for above 500 *m* and (b) and (d) for below, for potential temperature and salinity, respectively. The area bounded by the black box in Fig. 3 is from 42 to 42.5 °N and from 4.25 to 5 °E. The vertical column of water within this bounding box is spatially averaged to study the temporal trends in Sec. 4, and is therefore a relevant area to investigate for major biases. Within this box, the bias follows the trends found in Fig. 2: fresher and warmer water at the surface and fairly accurate at the lower layers. As we look at the whole vertical column for our study, we therefore believe the model results to be representative enough for our purpose of studying deep convection over multiple years.



## 4 Results and Discussion

### 4.1 Seasonal Contribution

The center of the minimum point of stratification in the GOL varies from year to year. To compare the destratification from different years to each other, an area encompassing the minimum point over the 20 years was averaged: a box with the limits of 42 to 42.5 ° N and 4.25 to 5 ° E (shown in Fig. 3). Seven years featured deep convection events in the model results of the control set: 1999, 2000, 2005, 2009, 2011, 2012, and 2013, shown by the significantly deep mixed layer depths (MLD) (in Fig. 4; the years are highlighted with green text). This is in agreement with Somot et al. (2016) but in disagreement with observations shown in Bosse et al. (2021) and Houpert et al. (2016). Observations showed deep convection also occurred in 2010, but, as seen in Fig. 5 and Fig. 7, our results show similar levels of stratification for 2010 as the adjacent years, therefore capturing some of the behavior despite deep convection not occurring in the model. Our years of deep convection had the lowest stratification levels during convection, according to the stratification index (Fig. 5), as expected (for the rest of the article, deep-convection years will refer to the deep-convection years found in the model results). Ideally, the stratification would be zero to denote a deep convection event. However, due to the area-averaging, some still stratified columns are captured, resulting in some remaining stratification at the  $SI$  minimum for years with deep convection. This is particularly apparent for the year of 2009, a deep-convection year, that has some remaining stratification larger than the following years, due to 2009 having a deep-convection zone with a relatively small horizontal extent (not shown).

The lack of deep convection in the seasonal set of simulations is immediately noticeable; the MLD for the seasonal runs never reached deeper than 173 *m* (Fig. 4), regardless of the year. This confirms that the Mistral component is necessary for deep convection, as found for the winter of 2013 in Keller Jr. et al. (2022). However, there is a large variability of  $SI_S$ . For example, for the winter of 2000 (referring to the winter spanning 1999 to 2000), the seasonal stratification closely follows the total stratification, whereas the next winter, the winter of 2001, the seasonal stratification diverges quite strongly in Feb. 2001 and remains diverged until June 2001 (Fig. 5). To compare the variability between the different years, the seasonal and Mistral contributions,  $SI_{S,Cont}$  and  $\delta SI_{Cont}$ , respectively, are determined according to Fig. 6. The contributions are determined at the time where the total stratification reaches a minimum,  $t_{SI_{min}}$ , as this is where deep convection occurs in the years that feature an event. This allows us to separate the contribution to destratification at each timescale:

$$SI_{S,Cont} = SI_{S,max} - SI_S(t = t_{SI_{min}}) \quad (12)$$

$$\delta SI_{Cont} = SI_S(t = t_{SI_{min}}) - SI_{min} \quad (13)$$

The maximum  $SI_S$  is used as the reference point for the maximum stratification, at  $t_{SI_{S,max}}$ , as the seasonal stratification maximum is the overall stratification that both the Mistral and seasonal atmospheric change must overcome to cause deep convection. Consequently, the time  $t_{SI_{S,max}}$  is taken to be the time the preconditioning phase begins, and the time  $t_{SI_{min}}$  where it ends.

The varying levels of contributions and maximum levels of seasonal stratification,  $SI_{S,max}$ , are displayed in Fig. 7. We can see in Fig. 7 (a) that the years with deep convection have maximum seasonal stratification levels that are below average for the 20 year period (deep-convection (DC) years are denoted by the hatching). If we look at the separated contributions in subplots (b) and (c) of the same figure, the years with deep convection typically feature higher than average levels of destratification coming from the seasonal contribution, with most of the destratification in 2012 coming from the sea-

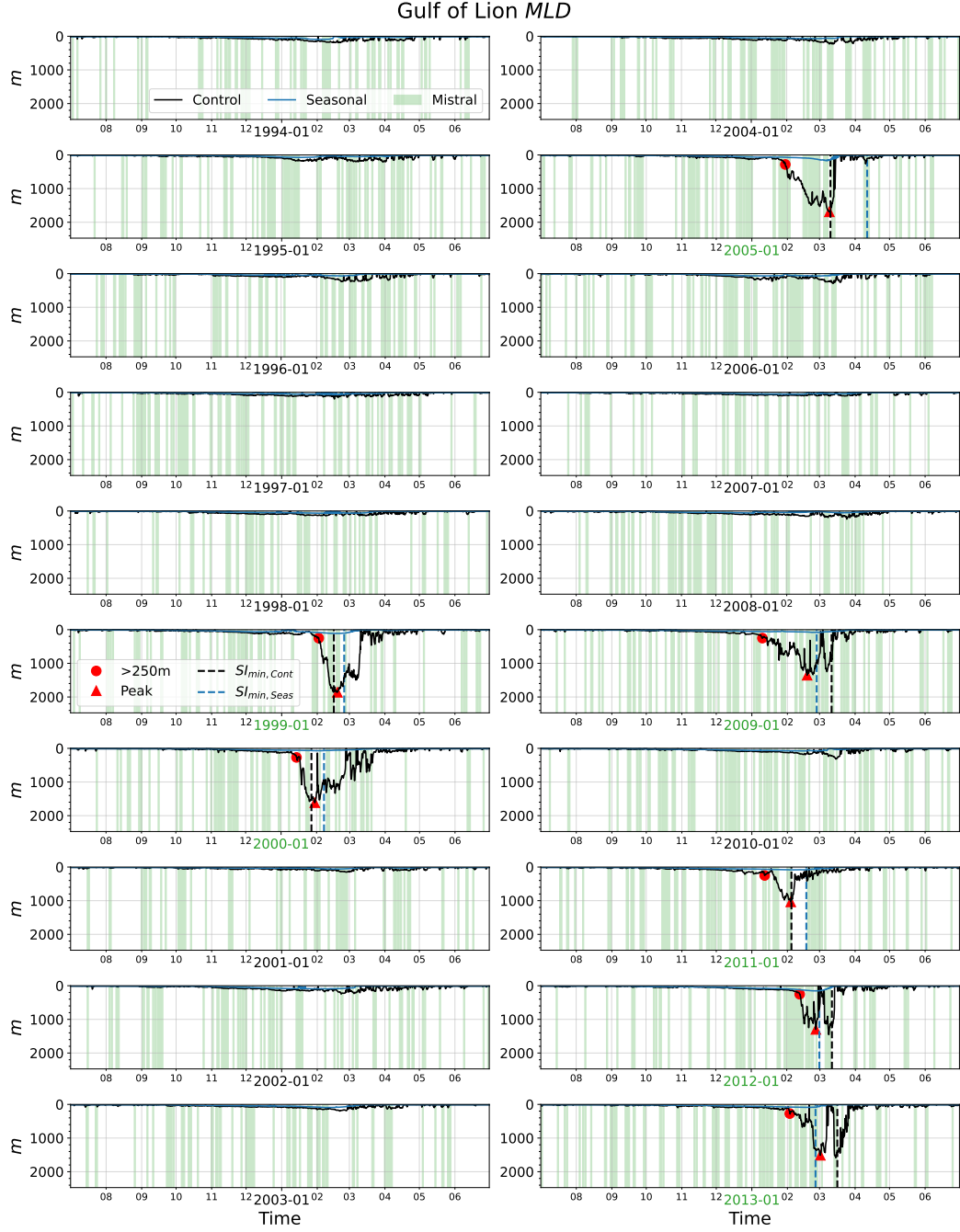


**Figure 4.** Mixed layer depth of the averaged area in Fig. 3 for the 20 years, calculated by the point in the column with a vertical diffusivity less than  $5 \times 10^{-4} \text{ m}^2/\text{s}$ . The red circle labels the first point at which the MLD is deeper than 250m and the red triangle marks the first main maximum depth for the deep-convection years. Mistral events are shown with the colored green shading.

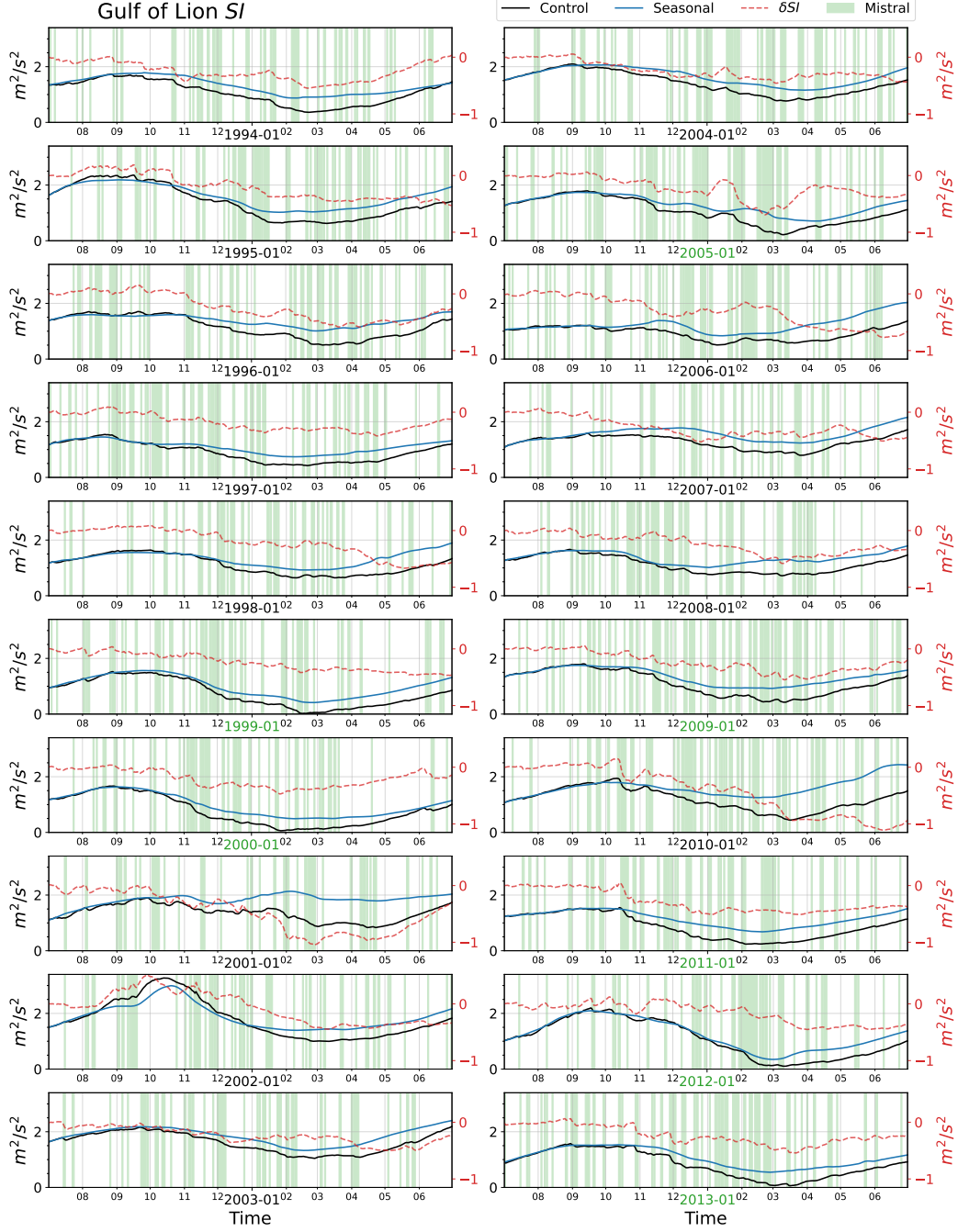


**Figure 5.** The stratification index of the area averaged in Fig. 3 for the 20 years, with the control run,  $SI_S + \delta SI$ , in black and the seasonal run,  $SI_S$ , in blue. The difference between the control and seasonal stratification index,  $\delta SI$ , is shown with a dashed red line with a separate scale. Mistral events are shown with the colored green shading.

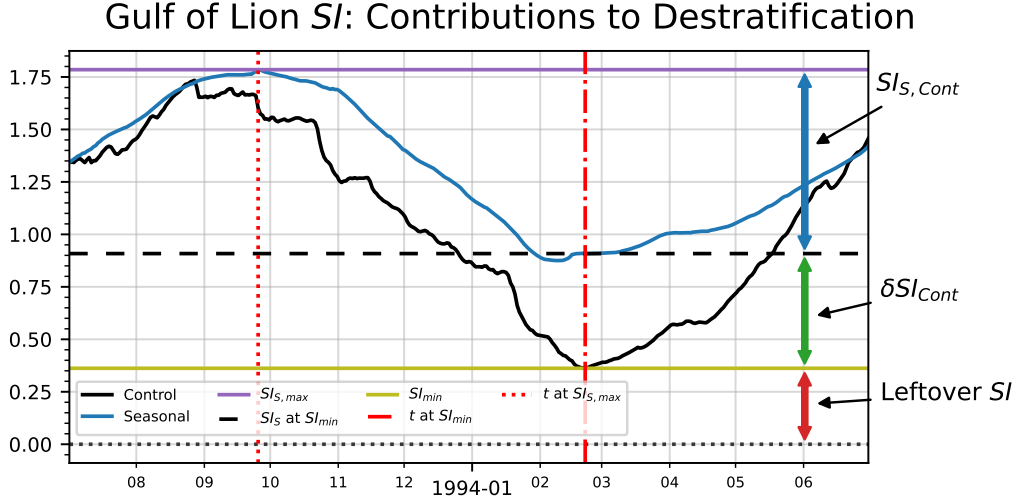


**Figure 6.** The stratification index for the winter of 1994 to demonstrate how the contributions from the different timescales are calculated.

**Table 2.** Statistics for the normalized  $SI_{S,Cont}$  and  $\delta SI_{Cont}$  contributions from Fig. 7 (c) and (d).

	MEAN		STD		MIN		MAX	
	$SI_{S,Cont}$	$\delta SI_{Cont}$	$SI_{S,Cont}$	$\delta SI_{Cont}$	$SI_{S,Cont}$	$\delta SI_{Cont}$	$SI_{S,Cont}$	$\delta SI_{Cont}$
DC	0.618	0.287	0.115	0.063	0.446	0.146	0.805	0.349
NDC	0.370	0.276	0.122	0.114	0.104	0.137	0.519	0.518
All	0.457	0.280	0.169	0.099	0.104	0.137	0.805	0.518

sonal timescale. For the Mistral timescale contributions, years with deep convection also saw above average levels, except for the year of 2012. A key note of interest is the average levels of contribution from the two timescales. On average, the seasonal timescale provides 45.7% of the annual destratification, with the Mistral timescale providing only 28.0% of the annual destratification. This agrees with the results of Keller Jr. et al. (2022). Taken a step further, the mean values for the different normalized timescale contributions separated by DC and non-deep-convection (NDC) years are provided in Table 2. Corroborating the observations made above in Fig. 7, DC seasonal contributions exceeded the overall average: 0.618 versus 0.457. The distinction between DC Mistral contributions and the overall average is less clear however: 0.287 versus 0.280, as the contribution for the year of 2012 reduces the mean significantly for DC years.

#### 4.1.1 Components of the Seasonal Contribution

As the variability of the seasonal contribution,  $SI_{S,Cont}$ , plays a key role in the occurrence of deep convection, it was separated into the different surface heat flux components, as described by Eq. 10, with  $t_0 = t_{SI_{S,max}}$  and  $t_1 = t_{SI_{S,min}}$ . The distributions of the different flux components over the years are shown in Fig. 8 (a), with DC years colored in blue and NDC years colored in red. What Fig. 8 (a) conveys, is that the years with increased latent,  $Q_E$ , and sensible,  $Q_H$ , heat fluxes during the preconditioning period are the years with deep convection. This is seen by the differences in the mean values for each subgroup ( $\overline{DC} - \overline{NDC}$ ): 0.04, -0.11, -0.17, and -0.43 for  $Q_{SW}$ ,  $Q_{LW}$ ,

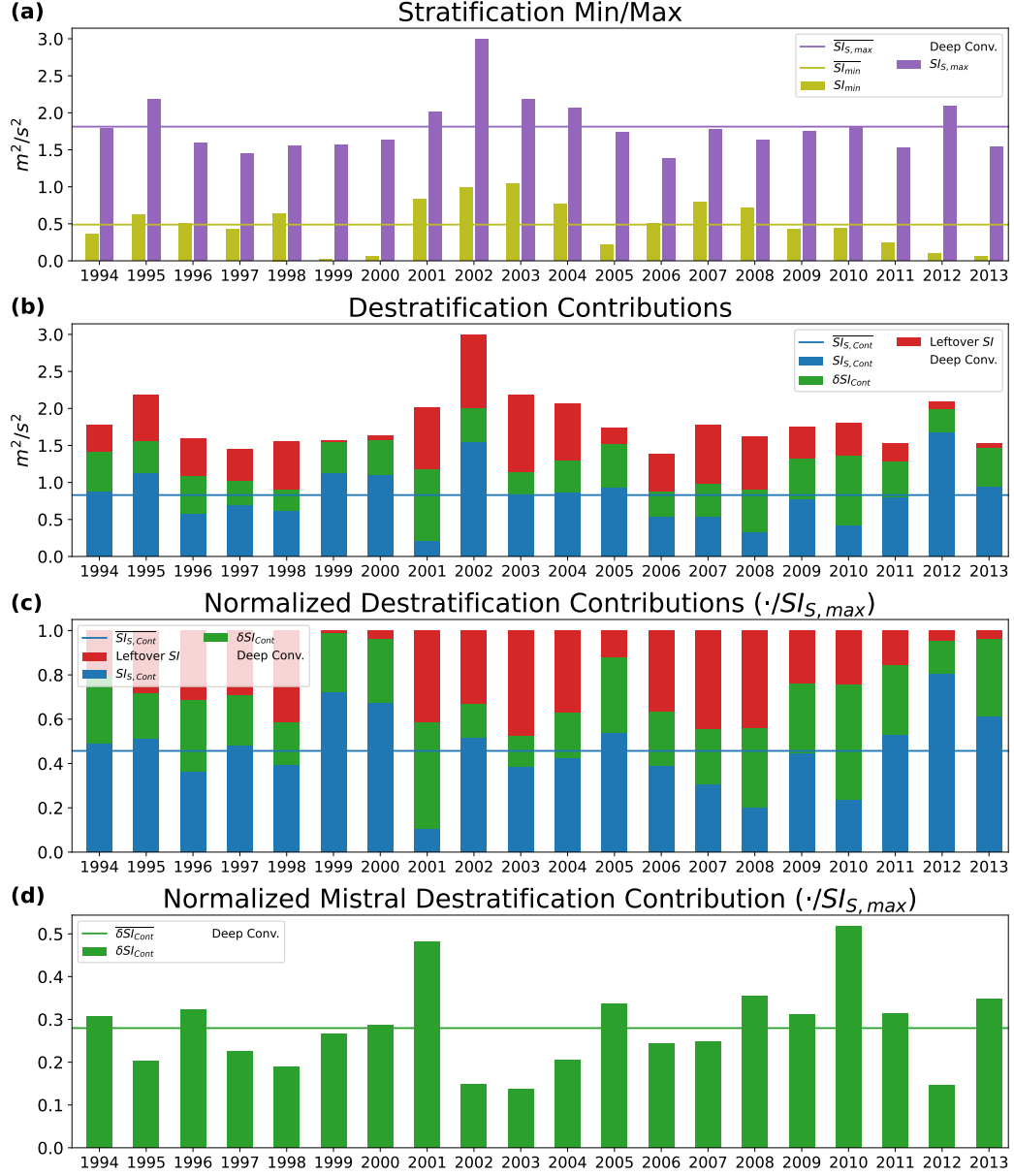


**Figure 7.** The seasonal maximum stratification and minimum control stratification is shown in subplot (a). The seasonal and Mistral contributions are shown in (b) and (c) (normalized in (c)). (d) shows just the normalized Mistral contribution to destratification.

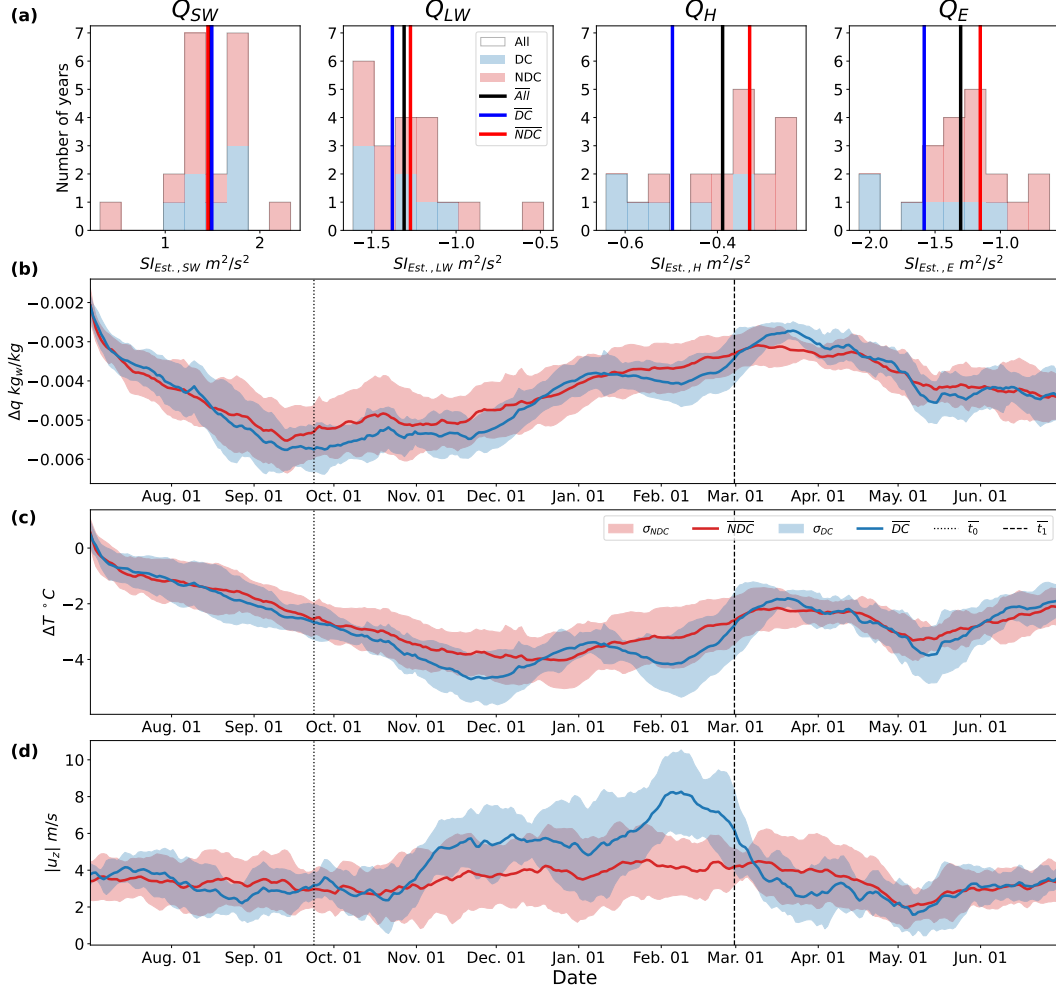


**Figure 8.** Distributions of the different flux components making the stratification change in  $SI_S$ , determined using Eq. 10 per component,  $i$ , are shown in subplot (a).  $DC$  and  $NDC$  stand for deep-convection and non-deep-convection, respectively. Subplots (b), (c), and (d) show the ensemble averaged (discarding Feb. 29th from leap years) driving components of the flux bulk formulae in Eq. 4,  $\Delta q$ ,  $\Delta T$ , and  $|u_z|$ .

$Q_H$ , and  $Q_E$ , respectively. Initially, it appears that the longwave upward radiation also acts as an indicator for years with deep convection. However, if we normalize these differences by the average value of all of the years for each component  $((\overline{DC} - \overline{NDC})/\overline{All})$ , then we can easily identify the sensible and latent heat fluxes as the main indicators: 0.03, 0.08, **0.43**, and **0.33** (in the same order as the previous list).

To determine which atmospheric component drove the differences evident in the latent and sensible heat fluxes,  $\Delta q$ ,  $\Delta T$ , and the wind speed ( $|\Delta u| \approx |u_z|$ , as the sea surface current is typically very small relative to the wind speed; typically  $\mathcal{O}(mm/s)$  vs  $\mathcal{O}(m/s)$ , respectively) was ensemble averaged for DC and NDC years (blue and red, respectively). These values were selected as they are the atmospheric components found in Eq. 4 used to calculate the latent and sensible heat fluxes. The ensemble averaging is shown in Fig. 8 subplots (b), (c), and (d), respectively. While there are differences in both  $\Delta q$  and  $\Delta T$  between DC and NDC years, the wind speed,  $|u_z|$  is the main differentiator between the two groups of years.

**Table 3.** Estimated changes in destratification due to changing one variable at a time (between  $\Delta q$ ,  $\Delta T$ , and  $|u_z|$ ) to DC versus NDC ensemble averaged values, utilizing Eq. 14. Note, the saturation humidity is based on sea surface temperature, which means keeping the temperature at NDC ensemble averaged values is technically non-physical, as the saturation humidity would change with a different air temperature.

$j$	$\Delta SI_{Est,E,j} \text{ m}^2/\text{s}^2$	$\Delta SI_{Est,H,j} \text{ m}^2/\text{s}^2$	Total $\text{m}^2/\text{s}^2$
$\Delta q$	-0.066	-0	-0.066
$\Delta T$	-0	-0.042	-0.042
$ u_z $	-0.322	-0.102	-0.424

To better demonstrate  $|u_z|$  as the main differentiator, a sensitivity analysis was performed by estimating the change in destratification due to the latent and sensible heat fluxes, with either the DC or NDC ensemble averaged values for  $\Delta q$ ,  $\Delta T$ , and  $|u_z|$ . Using Eq. 10, the change in the estimated destratification due to changes in  $Q_E$  and  $Q_H$  can be calculated as:

$$\Delta SI_{Est,i,j} = 10^{-9} \times \int_{t_0}^{t_1} \Delta Q_{i,j} dt \quad (14)$$

Where  $\Delta Q_{i,j} = Q_{i,j} - Q_{i,Ref}$ .  $i$  is either  $E$  or  $H$  for the latent and sensible heat flux, respectively, and  $j$  is either  $\Delta q$ ,  $\Delta T$ , or  $|u_z|$ . Here,  $j$  stands for the variable changed to the DC ensemble averaged value (denoted by the subscript  $DC$ ), setting the remaining variables to the NDC ensemble averaged values (denoted by the subscript  $NDC$ ).  $Q_{i,Ref}$  has all variables set to the NDC ensemble averaged values. For example,  $\Delta Q_{E,\Delta q}$  would be:

$$\Delta Q_{E,\Delta q} = Q_{E,\Delta q} - Q_{Ref} = \rho_{a,0} \Lambda C_E (\Delta q_{DC}) |u_z|_{NDC} - \rho_{a,0} \Lambda C_E (\Delta q_{NDC}) |u_z|_{NDC}$$

We can then determine the direct influence DC ensemble averaged values for  $\Delta q$ ,  $\Delta T$ , and  $|u_z|$  have on destratification. The results of this analysis are found in Table 3. As  $|u_z|$  influences both  $Q_E$  and  $Q_H$ , it easily makes a larger difference in terms of destratification than either  $\Delta q$  or  $\Delta T$ :  $-0.424 \text{ m}^2 \text{s}^{-2}$  versus  $-0.066 \text{ m}^2 \text{s}^{-2}$  and  $-0.042 \text{ m}^2 \text{s}^{-2}$ , respectively.

The source of this difference in wind speed between DC and NDC years obfuscates the distinction between seasonal and Mistral contributions, however. The filtering, as discussed in Keller Jr. et al. (2022) and in Sec. 2.2, primarily removes the high frequency component of the Mistral. However, as also pointed out, the Mistral has a low frequency seasonal component as well, with more frequent and stronger Mistrals occurring in winter versus summer (see Givon et al. (2021) for a more complete analysis). With the moving average window, this low frequency component is partially filtered out, removing some of the Mistral's low frequency component (when viewed in the spectral domain), however part of it still remains. This remaining part is the overall increase in the mean wind speed during the winter months due to more frequent Mistral events, and hence appears in the seasonal forcing. The percentage of the preconditioning days ( $t_{SI_{S,max}}$  to  $t_{SI_{min}}$ ) that feature a Mistral event is consistent with this observation, with DC years at 34.3% and NDC years at 28.6%.

## 4.2 Prior Questions

As mentioned in the introduction, in Keller Jr. et al. (2022) a few questions were posed that couldn't be answered by the scope of that study. We will readdress them here.

### 4.2.1 Does the Mistral trigger deep convection, or does the seasonal change trigger it?

To determine if the Mistral or seasonal change triggered deep convection in our study, we first located the main growth phase of the MLD during deep convection. The main growth phase was chosen to be the first point in time at which the MLD became deeper than 250 m (labeled by a red circle in Fig. 4 for DC years) to the point at which the MLD reaches its first maximum (first if two major peaks were present, such as for the years of 2009, 2012, and 2013, otherwise the overall maximum was used; labeled by a red triangle in Fig. 4 for the same years). Then the ratio of the averaged gradient, with respect to time, of  $\delta SI$  and  $SI_S$  ( $\overline{\partial_t \delta SI} / \overline{\partial_t SI_S}$ ) was computed for this growth phase for each DC year. The years of 2000, 2009, and 2013 saw a larger destratifying contribution from the Mistral component than the seasonal component, with ratios greater than unity: 1.45, 4.71, and 2.15, respectively. This demonstrates that the Mistral was the main triggering component for these years. However, for the years of 1999, 2005, 2011, and 2012, the seasonal component was the main triggering agent, with ratios less than unity: 0.43, 0.40, 0.18, and 0.05, respectively. This means both the Mistral and seasonal component trigger deep convection in roughly equal amounts of our studied DC years.

### 4.2.2 Does the maximum $SI_S$ play a role in deep convection?

According to our results, the maximum  $SI_S$  does play a role. As previously pointed out, DC years are almost entirely years with a lower than average  $SI_S$  maximum (except for 2012). Which is intuitive, as a larger maximum of  $SI_S$  means that both the seasonal component and Mistral component must overcome a larger amount of stratification to form deep convection. However, more importantly, years with above average  $SI_{S,Cont}$  are more often than not, DC years. We saw the origin of this difference in Fig. 8 and Table 2, in the difference of wind speed. This means that the seasonal contribution to destratification, through the wind speed, has a particularly important role in the overall destratification of the GOL, as well as the seasonal maximum stratification it must overcome.

### 4.2.3 Does the timing of the $SI_S$ minimum matter and can the Mistral contribution overcome a restratifying $SI_S$ ?

The third question, broken down into a few separate yet related questions, poses: does the timing of the  $SI_S$  minimum matter? Can the Mistral,  $\delta SI$ , overcome the restratifying  $SI_S$ ? Or, in other words, do any of the deep convection events occur after the  $SI_S$  minimum?

For our results, three of the seven DC years (2009, 2012, and 2013) experienced a control  $SI$  minimum that occurred after the  $SI_S$  minimum (vertical dashed lines in Fig. 4). In each of these three years, according to the MLD (Fig. 4), deep convection ceased temporarily between the control and seasonal stratification minimum. Then deep convection resumed with an additional peak in the MLD before the control  $SI$  reached its minimum. This means that the Mistral can overcome a restratifying  $SI_S$  to continue deep convection. However, it is unclear whether or not it can trigger deep convection after the seasonal minimum, as our model results don't feature such an example.

While a larger dataset of deep convection events will be required to more definitively answer this question, we can infer that the case of triggering deep convection af-



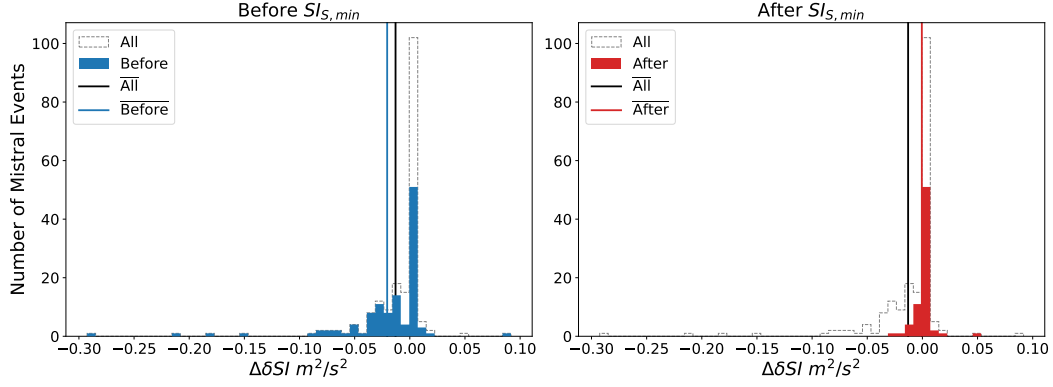


**Figure 9.** Distributions of the destratification incurred by Mistral events during DC years.  $\Delta\delta SI$  is calculated using Eq. 11 per event  $k$ .

ter or continuing it beyond the  $SI_S$  minimum will be rarer than the case of the control  $SI$  minimum occurring before the  $SI_S$  minimum. This is due to a weakening contribution from Mistral events as the preconditioning period occurs. Eq. 19 of Keller Jr. et al. (2022) shows that succeeding Mistral events need to be stronger than the current level of destratification to cause more destratification. When the year transitions out of the preconditioning period into the summer (essentially after the  $SI_S$  minimum), Mistral events destratify less because the water column has already incurred a significant amount of destratification. We can see this change by looking at the destratification caused by individual Mistral events depending on their timing with Eq. 11. The results are shown in Fig. 9. Events before the  $SI_S$  minimum exhibit a wider spread in terms of destratification, but also have a mean destratification ( $-0.021 \text{ m}^2\text{s}^{-2}$ ) that is less than the events that occur after the minimum ( $-0.001 \text{ m}^2\text{s}^{-2}$ ). This limits the likelihood that Mistral events can overcome a restratifying  $SI_S$ .

#### 4.2.4 Does the previous year's level of stratification affect the proceeding year?

For our results, five of the seven DC years occurred adjacently: the years of 1999 and 2000 occurred together and the years 2011 to 2013 occurred together as well. Otherwise, the two remaining years were in between two NDC years. This seems to suggest DC years occur consecutively, which intuitively makes sense, as the water column following a deep convection event will have had a significant amount of heat removed from it (resulting in buoyancy loss, driving destratification). This heat must be re-injected into the water column to restratify it, whereas years with persisting stratification don't need this initial addition of heat. However, the newly formed dense water post deep convection must also vacate before the following winter. If the newly formed dense water is unable to vacate due to mesoscale flow patterns, this dense water will increase the density gradient in the GOL after restratification due to advection occurs, increasing the stratification of the water column. Then the following winter must provide enough buoyancy loss to reduce the density of the surface waters to match the dense water before convection can occur. Therefore there is a balance between the mobility of the newly formed dense water and the surface buoyancy loss forming the dense water to promote a setting for future deep convection events to occur.

Returning to our results, however, in terms of stratification (through the stratification index and contributions derived from the  $SI$ ), there doesn't appear to be any discernible pattern or trend for the 20 year period. A larger scoped study that investigates

additional features, such as the composition of the formed dense water masses (e.g. the saltier dense water formed during the 2005 deep convection event (Herrmann et al., 2010)), the long term trends of said composition (Houpert et al., 2016), or changes in the Med. Sea circulation (Amitai et al., 2021), may be able to provide more answers. For example, the study of Parras-Berrocal et al. (2022) found that increasingly saline Levantine Intermediate Water and freshening Inflow Atlantic Water at the Strait of Gibraltar leads to increasing stratification in the GOL for climatic scenario runs up to the year 2100.

## 5 Conclusions

Our study investigated deep convection in the GOL over a 20 year period, using the NEMO ocean model forced by filtered and unfiltered RegIPSL WRF/ORCHIDEA atmospheric data. By looking at the difference between the two sets of ocean simulation results forced by the two different forcings, we could extract the effect the Mistral and seasonal atmospheric change had on the annual stratification cycle of the GOL. The control model results represented reality fairly well with respect to Argo and CTD profiling. While deep convection occurs in only seven of the 20 years in the model results, whereas it occurs in eight of the 20 years in observations (Houpert et al., 2016; Bosse et al., 2021), we were able to extract information regarding the impact of the seasonal atmospheric change on destratification. We found the seasonal contribution to be the main driver in terms of destratification during the preconditioning period, with it being larger during DC years. When breaking down what causes destratification in the seasonal contribution, we found the latent and sensible heat fluxes to be most important components, shifting more negative during DC years. It was then found that the differences in the latent and sensible heat fluxes between DC and NDC years were caused by increased wind speeds during DC years. These increased wind speeds themselves were caused by the seasonal aspect of the occurrence of Mistral events, with more events occurring during the winters with deep convection.

When addressing the questions asked by Keller Jr. et al. (2022), we found that the Mistral and seasonal atmospheric change roughly trigger deep convection an equal number of times. It was also determined that the maximum  $SI_S$  an important quantity as it is the amount of stratification the seasonal and Mistral contributions must overcome to cause deep convection. Additionally, the Mistral contribution can overcome a restratifying  $SI_S$  to extend deep convection, however it is unlikely it can trigger deep convection after the  $SI_S$  minimum. Finally, there is a balance between the mobility of newly formed dense water and overall reduced heat content in the vertical column from a deep convection event. The reduced heat content allows for less cooling needed to destratify the water in the proceeding year, improving the likelihood of deep convection occurring. But any remaining dense water in the lower layers after the restratification phase can increase the density gradient, if it is unable to readily flow to other regions, inhibiting deep convection.

Our study shows the importance of the seasonal atmospheric change and its drivers on the deep convection cycle of the GOL. Future studies investigating the change in variability of the seasonal atmospheric forcing and vertical composition of the GOL waters with a warming atmosphere will be necessary to understand the evolution of deep convection in the GOL with a changing climate.

## Open Research

### 5.1 Software Availability Statement

The RegIPSL model can be found at <https://gitlab.in2p3.fr/ips1/lmd/intro/regips1/regips1>; last accessed: Aug. 26th, 2022. The NEMO model can be found at <https://www.nemo-ocean.eu/>; last accessed: August 16th, 2022. The code used to per-

form the analysis and produce the plots are available at [https://gitlab.com/dkllrjr/jgr\\_oceans\\_untangling\\_deep\\_conv\\_20\\_yrs\\_code](https://gitlab.com/dkllrjr/jgr_oceans_untangling_deep_conv_20_yrs_code); last accessed: Aug. 24th, 2022.

## 5.2 Data Availability Statement

The RegIPSL WRF/ORCHIDEE atmospheric forcing data is available from the authors of Guion et al. (2021) upon request. The NEMO simulation data performed in this article is available from the authors upon request. The Mistral event data is available at <https://medcyclones.utad.pt/data/>; last accessed Aug. 23rd, 2022 (Keller Jr. et al., 2022; Givon et al., 2021). The Argo and CTD data is available through the Coriolis database, available at <https://www.coriolis.eu.org/Data-Products/Data-selection>; last accessed: Aug. 23rd, 2022.

## Acknowledgments

This work is a contribution to the HyMeX program (HYdrological cycle in the Mediterranean EXperiment) through INSU-MISTRALS support and the MED-CORDEX program (COordinated Regional climate Downscaling EXperiment - Mediterranean region). It was also supported by a joint CNRS - Weizmann Institute of Science collaborative project.

## References

- Amitai, Y., Ashkenazy, Y., & Gildor, H. (2021, January). The Effect of the Source of Deep Water in the Eastern Mediterranean on Western Mediterranean Intermediate and Deep Water. *Frontiers in Marine Science*, 7(615975). doi: <https://doi.org/10.3389/fmars.2020.615975>
- Balmaseda, M. A., Trenberth, K. E., & Källén, E. (2013, may). Distinctive climate signals in reanalysis of global ocean heat content. *Geophysical Research Letters*, 40(9), 1754–1759. doi: 10.1002/grl.50382
- Beuvier, J., Béranger, K., Brossier, C. L., Somot, S., Sevault, F., Drillet, Y., ... Lyard, F. (2012, jul). Spreading of the western mediterranean deep water after winter 2005: Time scales and deep cyclone transport. *Journal of Geophysical Research: Oceans*, 117(C7), n/a–n/a. doi: 10.1029/2011jc007679
- Bosse, A., Testor, P., Damien, P., Estournel, C., Marsaleix, P., Mortier, L., ... Taillandier, V. (2021, mar). Wind-forced submesoscale symmetric instability around deep convection in the northwestern mediterranean sea. *Fluids*, 6(3), 123. doi: 10.3390/fluids6030123
- Coppola, L., Prieur, L., Taupier-Letage, I., Estournel, C., Testor, P., Lefevre, D., ... Taillandier, V. (2017, aug). Observation of oxygen ventilation into deep waters through targeted deployment of multiple argo-o2floats in the north-western mediterranean sea in 2013. *Journal of Geophysical Research: Oceans*, 122(8), 6325–6341. doi: 10.1002/2016jc012594
- Drobinski, P., Alonzo, B., Basdevant, C., Cocquerez, P., Doerenbecher, A., Fourrié, N., & Nuret, M. (2017, feb). Lagrangian dynamics of the mistral during the HyMeX SOP2. *Journal of Geophysical Research: Atmospheres*, 122(3), 1387–1402. doi: 10.1002/2016jd025530
- Drobinski, P., Ducrocq, V., Alpert, P., Anagnostou, E., Béranger, K., Borga, M., ... Wernli, H. (2014, jul). HyMeX: A 10-year multidisciplinary program on the mediterranean water cycle. *Bulletin of the American Meteorological Society*, 95(7), 1063–1082. doi: 10.1175/bams-d-12-00242.1
- Estournel, C., Testor, P., Damien, P., D'Ortenzio, F., Marsaleix, P., Conan, P., ... Prieur, L. (2016, jul). High resolution modeling of dense water formation in the north-western mediterranean during winter 2012–2013: Processes and budget. *Journal of Geophysical Research: Oceans*, 121(7), 5367–5392. doi: 10.1002/2016jc011935

- Firing, E., Filipe, Barna, A., & Abernathey, R. (2021). *Teos-10/gsw-python: v3.4.1.post0*. Zenodo. doi: 10.5281/ZENODO.5214122
- Flamant, C. (2003, feb). Alpine lee cyclogenesis influence on air-sea heat exchanges and marine atmospheric boundary layer thermodynamics over the western mediterranean during a tramontane/mistral event. *Journal of Geophysical Research: Oceans*, 108(C2), n/a–n/a. doi: 10.1029/2001jc001040
- Gascard, J. C. (1978). Mediterranean deep water formation baroclinic instability and oceanic eddies. *Oceanologica Acta*.
- Givon, Y., Jr., D. K., Pennel, R., Drobinski, P., & Raveh-Rubin, S. (2021, jan). Synoptic-scale drivers of the mistral wind: link to rossby wave life cycles and seasonal variability. (accepted) doi: 10.5194/wcd-2021-7
- Guion, A., Turquety, S., Polcher, J., Pennel, R., Bastin, S., & Arsouze, T. (2021). Droughts and heatwaves in the western mediterranean: impact on vegetation and wildfires using the coupled wrf-orchidee regional model (regips). *Climate Dynamics*. (in review)
- Hamon, M., Beuvier, J., Somot, S., Lellouche, J.-M., Greiner, E., Jordà, G., ... Drillet, Y. (2016, apr). Design and validation of MEDRYS, a mediterranean sea reanalysis over the period 1992–2013. *Ocean Science*, 12(2), 577–599. doi: 10.5194/os-12-577-2016
- Herrmann, M., Sevault, F., Beuvier, J., & Somot, S. (2010, dec). What induced the exceptional 2005 convection event in the northwestern mediterranean basin? answers from a modeling study. *Journal of Geophysical Research*, 115(C12). doi: 10.1029/2010jc006162
- Houpert, L., de Madron, X. D., Testor, P., Bosse, A., D'Ortenzio, F., Bouin, M. N., ... Raimbault, P. (2016, nov). Observations of open-ocean deep convection in the northwestern mediterranean sea: Seasonal and interannual variability of mixing and deep water masses for the 2007–2013 period. *Journal of Geophysical Research: Oceans*, 121(11), 8139–8171. doi: 10.1002/2016jc011857
- Keller Jr., D., Givon, Y., Pennel, R., Raveh-Rubin, S., & Drobinski, P. (2022, apr). Untangling the mistral and seasonal atmospheric forcing driving deep convection in the Gulf of Lion: 2012–2013. *Ocean Science*, 18(2), 483–510. doi: 10.5194/os-18-483-2022
- Krinner, G., Viovy, N., de Noblet-Ducoudré, N., Ogée, J., Polcher, J., Friedlingstein, P., ... Prentice, I. C. (2005, feb). A dynamic global vegetation model for studies of the coupled atmosphere-biosphere system. *Global Biogeochemical Cycles*, 19(1). doi: 10.1029/2003gb002199
- Large, W., & Yeager, S. (2004). *Diurnal to decadal global forcing for ocean and sea-ice models: The data sets and flux climatologies* (Tech. Rep.). doi: 10.5065/D6KK98Q6
- Large, W. G., & Yeager, S. G. (2008, aug). The global climatology of an interannually varying air-sea flux data set. *Climate Dynamics*, 33(2-3), 341–364. doi: 10.1007/s00382-008-0441-3
- Lebeaupin-Brossier, C., Béranger, K., Deltel, C., & Drobinski, P. (2011, jan). The mediterranean response to different space-time resolution atmospheric forcings using perpetual mode sensitivity simulations. *Ocean Modelling*, 36(1-2), 1–25. doi: 10.1016/j.ocemod.2010.10.008
- Lebeaupin-Brossier, C., Béranger, K., & Drobinski, P. (2012, jan). Sensitivity of the northwestern mediterranean sea coastal and thermohaline circulations simulated by the 1/12°-resolution ocean model NEMO-MED12 to the spatial and temporal resolution of atmospheric forcing. *Ocean Modelling*, 43-44, 94–107. doi: 10.1016/j.ocemod.2011.12.007
- Lebeaupin-Brossier, C., & Drobinski, P. (2009, may). Numerical high-resolution air-sea coupling over the gulf of lions during two tramontane/mistral events. *Journal of Geophysical Research*, 114(D10). doi: 10.1029/2008jd011601

- Lebeaupin-Brossier, C., Léger, F., Giordani, H., Beuvier, J., Bouin, M.-N., Ducrocq, V., & Fourrié, N. (2017, jul). Dense water formation in the north-western mediterranean area during HyMeX-SOP2 in 1/36° ocean simulations: Ocean-atmosphere coupling impact. *Journal of Geophysical Research: Oceans*, 122(7), 5749–5773. doi: 10.1002/2016jc012526
- L'Hévéder, B., Li, L., Sevault, F., & Somot, S. (2012, sep). Interannual variability of deep convection in the northwestern mediterranean simulated with a coupled AORCM. *Climate Dynamics*, 41(3-4), 937–960. doi: 10.1007/s00382-012-1527-5
- Ludwig, W., Dumont, E., Meybeck, M., & Heussner, S. (2009, mar). River discharges of water and nutrients to the mediterranean and black sea: Major drivers for ecosystem changes during past and future decades? *Progress in Oceanography*, 80(3-4), 199–217. doi: 10.1016/j.pocean.2009.02.001
- Madec, G., Chartier, M., & Crépon, M. (1991, apr). The effect of thermohaline forcing variability on deep water formation in the western mediterranean sea: a high-resolution three-dimensional numerical study. *Dynamics of Atmospheres and Oceans*, 15(3-5), 301–332. doi: 10.1016/0377-0265(91)90024-a
- Madec, G., Delecluse, P., Crepon, M., & Chartier, M. (1991, sep). A three-dimensional numerical study of deep-water formation in the northwestern mediterranean sea. *Journal of Physical Oceanography*, 21(9), 1349–1371. doi: 10.1175/1520-0485(1991)021<1349:atdnso>2.0.co;2
- Madec, G., Lott, F., Delecluse, P., & Crépon, M. (1996, August). Large-scale preconditioning of deep-water formation in the northwestern mediterranean sea. *Journal of Physical Oceanography*, 26.
- Marshall, J., & Schott, F. (1999, feb). Open-ocean convection: Observations, theory, and models. *Reviews of Geophysics*, 37(1), 1–64. doi: 10.1029/98rg02739
- MEDOC. (1970, September). Observation of formation of deep water in the mediterranean sea, 1969. *Nature*, 227.
- Mertens, C., & Schott, F. (1998, jul). Interannual variability of deep-water formation in the northwestern mediterranean. *Journal of Physical Oceanography*, 28(7), 1410–1424. doi: 10.1175/1520-0485(1998)028<1410:ivodwf>2.0.co;2
- Millot, C., & Taupier-Letage, I. (2005). Circulation in the mediterranean sea. In *The mediterranean sea* (pp. 29–66). Springer Berlin Heidelberg. doi: 10.1007/b107143
- Noh, Y., Cheon, W. G., & Raasch, S. (2003, jun). The role of preconditioning in the evolution of open-ocean deep convection. *Journal of Physical Oceanography*, 33(6), 1145–1166. doi: 10.1175/1520-0485(2003)033<1145:tropit>2.0.co;2
- Parras-Berrocal, I. M., Vázquez, R., Cabos, W., Sein, D. V., Álvarez, O., Bruno, M., & Izquierdo, A. (2022, feb). Surface and intermediate water changes triggering the future collapse of deep water formation in the north western mediterranean. *Geophysical Research Letters*, 49(4). doi: 10.1029/2021gl095404
- Robinson, A., Leslie, W., Theocharis, A., & Lascaratos, A. (2001). Mediterranean sea circulation. In *Encyclopedia of ocean sciences* (pp. 1689–1705). Elsevier. doi: 10.1006/rwos.2001.0376
- Ruti, P. M., Somot, S., Giorgi, F., Dubois, C., Flaounas, E., Obermann, A., ... Vervatis, V. (2016, jul). Med-CORDEX initiative for mediterranean climate studies. *Bulletin of the American Meteorological Society*, 97(7), 1187–1208. doi: 10.1175/bams-d-14-00176.1
- Schott, F., Visbeck, M., Send, U., Fischer, J., Stramma, L., & Desaubies, Y. (1996, apr). Observations of deep convection in the gulf of lions, northern mediterranean, during the winter of 1991/92. *Journal of Physical Oceanography*, 26(4), 505–524. doi: 10.1175/1520-0485(1996)026<0505:oodcit>2.0.co;2
- Send, U., & Testor, P. (2017, dec). Direct observations reveal the deep circulation of the western mediterranean sea. *Journal of Geophysical Research: Oceans*, 122(12), 10091–10098. doi: 10.1002/2016jc012679

- Severin, T., Kessouri, F., Rembauville, M., Sánchez-Pérez, E. D., Oriol, L., Caparros, J., ... Conan, P. (2017, jun). Open-ocean convection process: A driver of the winter nutrient supply and the spring phytoplankton distribution in the northwestern mediterranean sea. *Journal of Geophysical Research: Oceans*, 122(6), 4587–4601. doi: 10.1002/2016jc012664
- Skamarock, W., Klemp, J., Dudhia, J., Gill, D., Barker, D., Wang, W., ... Duda, M. (2008). *A description of the advanced research wrf version 3* (Tech. Rep.). doi: 10.5065/D68S4MVH
- Somot, S. (2005). *Modélisation Climatique du Bassin Méditerranéen : Variabilité et Scénarios de Changement Climatique* (phdthesis). Université Toulouse III.
- Somot, S., Houpert, L., Sevault, F., Testor, P., Bosse, A., Taupier-Letage, I., ... Herrmann, M. (2016, aug). Characterizing, modelling and understanding the climate variability of the deep water formation in the northwestern mediterranean sea. *Climate Dynamics*, 51(3), 1179–1210. doi: 10.1007/s00382-016-3295-0
- Testor, P., & Gascard, J.-C. (2003, jan). Large-scale spreading of deep waters in the western mediterranean sea by submesoscale coherent eddies. *Journal of Physical Oceanography*, 33(1), 75–87. doi: 10.1175/1520-0485(2003)033<0075:lssodw>2.0.co;2
- The Lab Sea Group. (1998, oct). The labrador sea deep convection experiment. *Bulletin of the American Meteorological Society*, 79(10), 2033–2058. doi: 10.1175/1520-0477(1998)079<2033:tlsdce>2.0.co;2
- Turner, J. S. (1973). *Buoyancy Effects in Fluids* (U. of Cambridge, Ed.). Cambridge University Press.
- Waldman, R., Brüggemann, N., Bosse, A., Spall, M., Somot, S., & Sevault, F. (2018, aug). Overturning the mediterranean thermohaline circulation. *Geophysical Research Letters*, 45(16), 8407–8415. doi: 10.1029/2018gl078502